Manuscript submitted to
AIMS' Journals
Volume **X**, Number **0X**, XX **200X**

10.3934/xx.xx.xx.xx

pp. **X–XX**

ANALYTIC SENSING FOR MULTI-LAYER SPHERICAL MODELS WITH APPLICATION TO EEG SOURCE IMAGING

Djano Kandaswamy

École Polytechnique Fédérale de Lausanne (EPFL), Lausanne, Switzerland

Thierry Blu

Chinese University of Hong Kong, Shatin, Hong Kong

Dimitri Van De Ville

École Polytechnique Fédérale de Lausanne (EPFL), Lausanne, Switzerland
Université de Genève, Geneva, Switzerland

(Communicated by Naoki Saito)

Abstract. Source imaging maps back boundary measurements to underlying generators within the domain; e.g., retrieving the parameters of the generating dipoles from electrical potential measurements on the scalp such as in electroencephalography (EEG). Fitting such a parametric source model is non-linear in the positions of the sources and renewed interest in mathematical imaging has led to several promising approaches.

One important step in these methods is the application of a sensing principle that links the boundary measurements to volumetric information about the sources. This principle is based on the divergence theorem and a mathematical test function that needs to be an homogeneous solution of the governing equations (i.e., Poisson's equation). For a specific choice of the test function, we have devised an algebraic non-iterative source localization technique for which we have coined the term "analytic sensing".

Until now, this sensing principle has been applied to homogeneous-conductivity spherical models only. Here, we extend it for multi-layer spherical models that are commonly applied in EEG. We obtain a closed-form expression for the test function that can then be applied for subsequent localization. A simulation study show the feasibility of the proposed approach.

1. **Introduction.** Source imaging from boundary Cauchy data satisfying Poisson's equation is a classical inverse problem that is of high interest to many fields in engineering. In its most general setting, the problem is known to be ill-posed and additional assumptions about the source configuration need to be made to render the solution unique. Typically, one can restrict the class of source distributions by imposing spatial smoothness properties (e.g., Tikhonov regularization [37]) or by assuming a parametric source model.

Parametric source models are most useful when the source configurations are expected to be "well localized". This situation applies to some applications in electroencephalography (EEG). For example, focal brain activity that can be modeled

2010 *Mathematics Subject Classification.* Primary: 15A29, 35J05, 31B20; Secondary: 94A12, 94A20, 15A18.

Key words and phrases. Inverse problems, finite-rate-of-innovation, Poisson equation, boundary conditions.

as a superposition of a limited number of dipoles is often observed in averaged evoked potentials or in some cases of epileptic activity [27, 26].

Almost any source imaging technique performs (least-squares) data fitting by relying on the forward model, computing the boundary data for a given source configuration, and by iteratively updating the sources' parameters as part of an optimization process [28, 17]. However, the corresponding cost function has many local minima which makes the solution dependent on the initial guess, especially for multiple dipoles. Several toolboxes, commercial and non-commerical, such as EEGLAB (http://sccn.ucsd.edu/eeglab) and BESA (http://http://www.besa.de) do implement such localization methods. Therefore, successful recovery of the parametric sources is often limited to single-dipole models. Moreover, such methods are tedious and computationally intensive. As a consequence, methods based on neural networks have emerged [35]. Another family of source localization algorithms are the so-called subspace source localization methods; e.g., MUSIC [32, 30]. These methods rely heavily upon statistical tools such as principal component analysis, which are based on the estimation of second [6] or higher [10] order statistics.

On the other side, methods have also been proposed for underdetermined source distributions, including proper regularization; examples include beamforming approaches [36, 9] and Bayesian estimation techniques [41, 33].

The existence and uniqueness of multi-dipole models has been studied extensively [19], but there is a still a need for practical methods, especially for the non-linear fitting of the localization parameters. In particular, there is a renewed interest from the mathematical imaging community in providing new approaches based on non-linear methods. For example, Baratchart et al. proposed to solve the inverse problem analytically by so-called "best meromorphic approximation" [8, 7]. However, its extension to 3D requires going through many 2D localizations. Based on the divergence theorem, the sensing principle was introduced to relate the 3D boundary measurements to volumetric information on the sources [2, 3, 14, 31]; i.e., an auxiliary mathematical test function ("analytic sensor") needs to be an homogeneous solution of the governing equation of the physical system. In the case of homogeneous conductivity, the governing equation reduces to the Laplace equation and any polynomial in $(x + iy)$ and $(x - iy)$ is analytical and thus can be used for the sensing principle. In recent work [21], we put forward the "analytic sensing" framework that exploits the same concept, but with a specific choice of analytic sensors. This choice allows to subsequently deploy the principle of the annihilating filter, similar to the "finite rate of innovation" approach [11, 40], which renders the dipoles' positions in a non-iterative way. The reconstruction of the dipoles' moments reverts to solving a linear system of equations once the dipoles' positions are known. Although this algorithm has the advantages of decoupling the estimation of position and moment parameters, it assumes a spherical and homogeneous conductivity model. In many applications, including EEG, spherical multi-layer conductivity models are more useful [34, 29, 13, 4]. Moreover, the changes in conductivity of the outer layers can highly impact the localization error [39, 5]. Therefore, the assumption of homogeneity hinders the practical use of the original approach of analytic sensing.

There are basically two ways to overcome the limitations imposed by the homogeneous conductivity model:

- We propagate the measured boundary potential inward, that is, down to the boundary of the inner compartment [12, 1]. Although this propagation takes

into account the inhomogeneity of the conductivity model, it propagates the measurements corrupted with noise that will be amplified.
- We construct new analytic sensors that propagate to the outer boundary of the conductivity model. The propagation of the analytic sensor could be done numerically [24, 25], which has the advantage that it can cope with realistic head models. However, since the analytic sensor is known analytically to start with, we propose in this work to derive a closed-form expression of the propagated sensor, a method that does not introduce any approximation errors and leads to a fast and efficient algorithm.

We briefly revisit the sensing principle and then construct new analytic test functions that account for multi-layer spherical models with radially varying conductivity profiles, in particular, piecewise constant conductivities. Constructing such test functions boils down to solving a set of 3D differential equations that express the physical constraints of the conductivity model. We show how these equations can be solved using a particular separation of variables, hence, creating a new set of analytic sensors that account for layers of different constant conductivity. Finally, we show explicitly how to construct analytic sensors for the 3-sphere model with experimental results.

2. Analytic sensing revisited.

2.1. **Setup.** Let us consider a 3D closed conductor Ω with boundary $\partial\Omega$ and a source distribution ρ in Ω. The source distribution induces an electrical potential V such that [16]:

$$\begin{aligned} \operatorname{div}(\sigma\nabla V) &= \rho, \quad \text{within } \Omega & (1)\\ \nabla V \cdot \mathbf{e}_\Omega &= 0, \quad \text{on } \partial\Omega. & (2) \end{aligned}$$

where σ expresses the conductivity profile of Ω and $\mathbf{e}_\Omega$ is the outward normal to $\partial\Omega$. When σ is constant, (1) is equivalent to Laplace's equation.

Many physical problems can be modeled using (1), in particular electrostatic problems. In this paper, we assume that $\sigma(r)$ is a piecewise constant function of $r = \sqrt{x^2+y^2+z^2}$ (whereas we will denote the spatial position as $\mathbf{x} = [x, y, z]^T$), in particular, the N-sphere head model as depicted in Fig. 1. The inverse problem at hand is to estimate ρ knowing σ and the boundary potential $V\big|_{\partial\Omega}$.

2.2. **Sensing the source distribution.** The sensing principle takes advantage of the divergence theorem to compute the scalar products $\langle\psi, \rho\rangle$, knowing only $V\big|_{\partial\Omega}$. These scalar products can be seen as "generalized measures" of the unknown source distribution and are computed using the following boundary integral:

$$\langle\psi, \rho\rangle = -\oint_{\partial\Omega} \sigma V \nabla\psi \cdot \mathbf{e}_\Omega ds. \tag{3}$$

These analytic sensors ψ need to satisfy the key property

$$\operatorname{div}(\sigma\nabla\psi) = 0, \quad \text{within } \Omega, \tag{4}$$

which ensures that the generalized measures can be computed as stated in (3).

These analytic sensors allow sampling the boundary potential in a well-chosen way; i.e., each analytic sensor leads to a "generalized measure". Ideally, we would like a measurement device that behaves equivalently to integration with the analytic sensor, but in the absence of such instrumentation, we perform the integration based on regular boundary measurements.

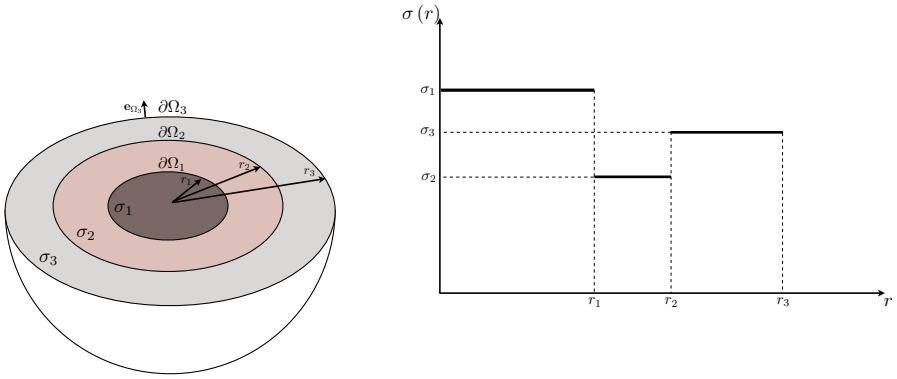

(a) (b)

FIGURE 1. (a) Three-sphere conductivity model where each compartment, Ω_i, has its own conductivity, σ_i, for $i \in \{1, \cdots, 3\}$. (b) Corresponding conductivity profile as a function of r (which is in this case a piecewise constant). Each discontinuity represents a boundary $\partial\Omega_1$, $\partial\Omega_2$ or $\partial\Omega_3$.

Until now, the sensing principle was applied to a conductivity model that is homogeneous; i.e., σ is constant and (4) reverts to the Laplace equation, $\Delta\psi = 0$, which is satisfied by functions of the variable $\zeta = x + iy$ that are analytical inside Ω. In this paper, we extend the sensing principle such that it can cope with a N-sphere conductivity model; i.e., given the desirable form of the analytic sensor in the compartment where the sources are located, we derive how to analytically propagate the test function to the boundary according to (4).

2.3. **Non-linear estimation for source localization.** In general, when no constraints on the source distribution ρ are imposed, reconstructing ρ from $V\big|_{\partial\Omega}$ is an ill-posed problem; i.e., many source distributions can generate the same measured boundary potenial [18]. Here we assume a parametric source model that consists of a limited number of current dipoles:

$$\rho(\mathbf{x}) = \sum_{m=1}^{M} \mathbf{p}_m \cdot \nabla\delta(\mathbf{x} - \mathbf{x}_m), \tag{5}$$

where $\mathbf{x}_m = [x_m, y_m, z_m]^T$ are the source positions and $\mathbf{p}_m = [p_{x,m}, p_{y,m}, p_{z,m}]^T$ are the moments. We further assume that all sources lie in the inner compartment of the head model where σ = constant (e.g., as depicted in figure 1). The source model (5) assures the identifiability and uniqueness of ρ when the boundary potential is known [19].

To apply previously proposed methods that rely on the sensing principle, it is sufficient to use the desired analytic sensor in the inner compartment, but the sensor needs to be propagated to the boundary to obtain the proper generalized measures. In [14], the analytic sensors were chosen to be polynomials of $(x + iy)$ and $(x - iy)$,

in particular,

$$\psi_n(x,y) = \sum_{k=1}^{K} c_k(x+iy)^k + c'_k(x-iy)^k. \tag{6}$$

Probing with different polynomial analytical sensors then allows to determine the unknowns, but one issue with these sensors is that they become rapidly numerically unstable as K grows. That is, for high values of K such polynomials require a computation accuracy exceeding that of usual scientific software (i.e., too large numerical dynamic range), which makes the numerical computation of (3) inaccurate.

Another approach is to revert to test functions that have a singularity, a, outside the head model, and consequently come with a certain amount of localization. This can be exploited for the application, e.g., to improve the sensitivity to "nearby" sources. In particular, in [21], we proposed the analytic sensor for point sources

$$\psi_{a_n}(x+iy) = \frac{1}{x+iy-a_n} \quad \text{for } x+iy \in \Omega_1, \tag{7}$$

with $a_n = \alpha \exp(in\theta)$ a singularity outside the head model, $\alpha > \mathbf{r_3}$, and $n = 0,\ldots,N-1$. As the singularity gets closer to the head, these sensors tend to be more localized, but also tend to be more sensitive to noise [21, Section 3.3].

In the case of current dipoles as stated in (5), the sensor is modified to

$$\psi_{a_n} = \log\big(1-(x+iy)/a_n\big) \quad \text{for } x+iy \in \Omega_1, \tag{8}$$

to preserve the special structure of the generalized measures, i.e., a fraction whose denominator is a polynomial whose roots are 2D projections of the dipoles' locations, as shown in (9). Note that these sensors satisfy (4) as well. When applying these sensors to reconstruct the source model (5) the corresponding generalized measures read

$$\begin{aligned} \langle \psi_{a_n}, \rho \rangle &= -\sum_{m=1}^{M} \frac{p_{x,m}+ip_{y,m}}{x_m+iy_m-a_n} \\ &= \frac{\sum_{m=0}^{M-1} c_m e^{imn\theta}}{\underbrace{\prod_{m=1}^{M}(x_m+iy_m-a_n)}_{\mathrm{R(a_n)}}}, \end{aligned} \tag{9}$$

with c_m some coefficient obtained by expressing $\langle \psi_{a_n}, \rho \rangle$ as a fraction with one common denominator. So the denominator is a polynomial R whose roots are $x_m + iy_m$, the 2-D projection of $\mathbf{x}_m$ on the complex plane. These generalized measures depend non-linearly on the source positions $x_m + iy_m$. Nevertheless, using an annihilation-filter approach, it is possible to retrieve the coefficients of the polynomial R and the positions x_m, y_m as its roots. The key to this solution is that the numerator of (9) is a sum of complex exponentials which can be annihilated by a known filter h, specified by the transfer function $H(z) = \prod_{k=0}^{M-1}\left(1-e^{ik\alpha}z^{-1}\right)$, as proven in [21]. Consequently, we have

$$h * (\langle \psi_{a_n}, \rho \rangle \, \mathrm{R}(a_n)) = 0, \quad n = 0,\ldots,N-1$$

which turns out to be a linear system of equations in the unknown coefficients of R. Finally, the generalized samples depend linearly on $p_{x,m} + ip_{y,m}$ and can be easily retrieved from the generalized samples once the positions are known. With

as few as $N = 2M$ (complex-valued) measurements $\langle \psi_{a_n}, \rho \rangle$ we can retrieve the (x, y) positions of M sources.

To retrieve the z-components of the locations and moments we could introduce a second set of test-functions $z\psi_{a_n}$. The corresponding generalized samples depend linearly on z and $p_{z,m}$ and are thus retrieved by solving

$$\langle z\psi_{a_n}, \rho \rangle = \sum_{m=1}^{M} -\frac{z_m(p_{x,m} + ip_{y,m})}{(x_m + iy_m - a_n)} - p_{z,m} \log\big(1 - (x_m + iy_m)/a_n\big),$$

for z_m and $p_{z,m}$. The mathematical and computational details of the method can be found in [21].

In this paper, we show how to propagate the test function through the multi-layer spherical model given its desired form in the inner compartment where the sources are located.

3. Extending the sensing principle for spherical head models.

3.1. Particular solutions of the continuity equation with radial conductivity.

The desired form of the analytic sensor in the inner compartment Ω_1, where the sources are located, is a desired function of ζ that allows to retrieve the sources subsequently. We will show that, because σ varies radially, a separation of variables in ζ and r reduces (4) to solving two decoupled differential equations.

Lemma 1. *If we assume that σ is $\mathcal{C}^1$ in some ring, then all analytic sensors ψ that satisfy*

$$\operatorname{div}(\sigma \nabla \psi) = 0$$

in that ring, and that can be put under the separable form

$$\psi(x, y, z) = \psi_0(\zeta)\psi_1(r),$$

where $\zeta = x + iy$ and $r = \sqrt{x^2 + y^2 + z^2}$, are solutions of the differential equations:

$$\zeta \psi_0'(\zeta) - n\psi_0(\zeta) = 0, \tag{10}$$

$$r\psi_1''(r) + \left(2(n+1) + \frac{r\sigma'}{\sigma}\right)\psi_1'(r) + n\frac{\sigma'}{\sigma}\psi_1(r) = 0, \tag{11}$$

where n is some scalar.

Proof. We look for a special solution taking the separable form:

$$\psi(x, y, z) = \psi_0(\zeta)\psi_1(r),$$

with $\zeta = x + iy$ and $\Delta\psi_0 = 0$.

Then, (4) takes the form:

$$\sigma' \mathbf{u}_r^T \nabla\psi + \sigma\Delta\psi = 0, \tag{12}$$

where $\mathbf{u}_r$ is the vector defined as

$$\mathbf{u}_r = \frac{1}{r}\begin{pmatrix} x \\ y \\ z \end{pmatrix}^T.$$

The first term of (12) can be further rewritten as:

$$\begin{aligned} \mathbf{u}_r^T \nabla\psi &= \psi_1 \mathbf{u}_r^T \nabla\psi_0 \mathbf{u}_r^T \nabla\psi_1 \\ &= \psi_1(r)\psi_0'(\zeta)\frac{\zeta}{r} + \psi_0(\zeta)\psi_1'(r), \end{aligned}$$

and second term as:

$$\begin{aligned}\Delta\psi &= \psi_0(\zeta)\Delta\psi_1(r) + 2\nabla\psi_0(\zeta)^T\nabla\psi_1(r) + \psi_1\Delta\psi_0(\zeta)\\ &= \psi_0(\zeta)\frac{r\psi_1''(r)+2\psi_1'(r)}{r} + 2\psi_0'(\zeta)\psi_1'(r)\frac{\zeta}{r}.\end{aligned}$$

Consequently (12) becomes

$$\underbrace{\sigma'(r)\psi_1(r)\psi_0'(\zeta)\frac{\zeta}{r} + \sigma'(r)\psi_0(\zeta)\psi_1'(r)}_{\sigma'\mathbf{u}_r^T\nabla\psi} + \underbrace{\sigma(r)\psi_0(\zeta)\frac{r\psi_1''(r)+2\psi_1'(r)}{r} + 2\sigma(r)\psi_0'(\zeta)\psi_1'(r)\frac{\zeta}{r}}_{\sigma\Delta\psi} = 0,$$

which can be separated into two parts, one that depends only on ζ, and another that depends only on r:

$$\frac{\zeta\psi_0'(\zeta)}{\psi_0(\zeta)} = -\frac{r\sigma'(r)\psi_1'(r) + \sigma(r)\left(r\psi_1''(r)+2\psi_1'(r)\right)}{\sigma'(r)\psi_1(r) + 2\sigma(r)\psi_1'(r)}. \tag{13}$$

The left-hand side (lhs) of (13) is a function of ζ whereas the right-hand side (rhs) is a function of r. These variables are independent which implies that lhs = rhs = Constant. This results into two decoupled differential equations:

$$\begin{aligned}\zeta\psi_0'(\zeta) - n\psi_0(\zeta) &= 0,\\ r\psi_1''(r) + \left(2(n+1) + \frac{r\sigma'}{\sigma}\right)\psi_1'(r) + n\frac{\sigma'}{\sigma}\psi_1(r) &= 0,\end{aligned}$$

which concludes the proof. □

The solution of (10) is $\psi_0 = \text{Constant}\times\zeta^n$ which is discontinuous or multivalued if $n \notin \mathbb{N}$. Hence we require n to be some positive integer. Thus, if ψ_1 is a function for which

$$r\psi_1''(r) + \left(2(n+1) + \frac{r\sigma'}{\sigma}\right)\psi_1'(r) + n\frac{\sigma'}{\sigma}\psi_1(r) = 0, \tag{14}$$

holds, then

$$\psi(x,y,z) = (x+iy)^n\psi_1(r), \quad n\in\mathbb{N}$$

is a valid test function.

Taking into account the N-sphere conductivity model, we have that in each region with constant σ

$$\psi(x,y,z) = C(x+iy)^n + C'\frac{(x+iy)^n}{r^{2n+1}},$$

with C and C' arbitrary constants. This means that, due to the linearity of the operator $\operatorname{div}(\sigma\nabla\cdot)$, any valid analytic sensor ψ, in a region where σ = Constant, must be of the form

$$\psi(x,y,z) = \varphi(x+iy) + \frac{1}{r}\Phi\left(\frac{x+iy}{r^2}\right),$$

where φ and Φ are analytic/holomorphic functions in that region. In order to fully characterize the analytic sensors that go with an N-sphere conductivity model, we need to describe the behavior (or rather change) of ψ at a boundary $\partial\Omega_j = \Omega_j\cap\Omega_{j+1}$ between two homogenous media, Ω_j and Ω_{j+1}. Note that, contrary to the usual practice, $\partial\Omega_j$ does not include the lower boundary of Ω_j at r_{j-1}.

Proposition 1. *If we know φ and Φ in a ring $\Omega_j = \{\mathbf{x} \in \mathbb{R}^3,\ s.t.\ r_{j-1} \leq \|\mathbf{x}\| \leq r_j\}$ of an N-sphere ($j = 1, 2, \ldots N$) conductivity model*

$$\begin{array}{ll} \varphi = \varphi_j & \text{in } \Omega_j \\ \Phi = \Phi_j & \text{in } \Omega_j \\ \sigma = \sigma_j & \text{in } \Omega_j \end{array}$$

then we can propagate φ_j and Φ_j through $\partial\Omega_j = \Omega_j \cap \Omega_{j+1}$, by solving the following two differential equations:

$$\frac{2\zeta}{r_j^3}\Phi'_{j+1}\left(\frac{\zeta}{r_j^2}\right) + \frac{1}{r_j}\Phi_{j+1}\left(\frac{\zeta}{r_j^2}\right) = -g_j(\zeta) + \zeta f'_j(\zeta), \tag{15}$$

$$\varphi_{j+1} = f_j(\zeta) - \frac{1}{r_j}\Phi_{j+1}\left(\frac{\zeta}{r_j^2}\right), \tag{16}$$

where

$$f_j(\zeta) = \varphi_j(\zeta) + \frac{1}{r_j}\Phi_j\left(\frac{\zeta}{r_j^2}\right), \tag{17}$$

$$g_j(\zeta) = \frac{\sigma_j}{\sigma_{j+1}}\left(\zeta\varphi'_j(\zeta) - \frac{1}{r_j}\Phi_j\left(\frac{\zeta}{r_j^2}\right) - \frac{\zeta}{r_j^3}\Phi'_j\left(\frac{\zeta}{r_j^2}\right)\right). \tag{18}$$

Proof. Using standard arguments frequent in electromagnetic physics, or using distribution theory, it is possible to show that, if σ and ψ are piecewise $\mathcal{C}^1$ satisfying $\operatorname{div}(\sigma\nabla\psi) = 0$ separately in the interiors of Ω_j and Ω_{j+1}, then

$$\left.\begin{array}{r} \psi \\ \sigma\mathbf{x}^T\nabla\psi \end{array}\right\} \text{are continuous across } \partial\Omega_j \quad \Longrightarrow \quad \operatorname{div}(\sigma\nabla\psi) = 0 \text{ in } \Omega_j \cup \Omega_{j+1}$$

- for the continuity of ψ at $\partial\Omega_j$

$$\varphi_j(\zeta) + \frac{1}{r_j}\Phi_j\left(\frac{\zeta}{r_j^2}\right) = \varphi_{j+1}(\zeta) + \frac{1}{r_j}\Phi_{j+1}\left(\frac{\zeta}{r_j^2}\right); \tag{19}$$

- for the continuity of $\sigma\mathbf{x}^T\nabla\psi$ at $\partial\Omega_j$

$$\begin{aligned} \sigma_j \quad & \left(\zeta\varphi'_j(\zeta) - \frac{1}{r_j}\Phi_j\left(\frac{\zeta}{r_j^2}\right) - \frac{\zeta}{r_j^3}\Phi'_j\left(\frac{\zeta}{r_j^2}\right)\right) = \\ & \sigma_{j+1}\left(\zeta\varphi'_{j+1}(\zeta) - \frac{1}{r_j}\Phi_{j+1}\left(\frac{\zeta}{r_j^2}\right) - \frac{\zeta}{r_j^3}\Phi'_{j+1}\left(\frac{\zeta}{r_j^2}\right)\right), \end{aligned} \tag{20}$$

for any ζ such that $||\zeta|| \leq r_j$. These two differential equations, (19) and (20), describe how a test function ψ changes (or rather propagates) through $\partial\Omega_j$. In what follows we show how to find φ_{j+1} and Φ_{j+1} from φ_j and Φ_j. This describes explicitly how the test function ψ propagates over a discontinuity of σ.

Let us define $f_j(\zeta)$ and $g_j(\zeta)$ to be:

$$f_j(\zeta) = \varphi_j(\zeta) + \frac{1}{r_j}\Phi_j\left(\frac{\zeta}{r_j^2}\right),$$

$$g_j(\zeta) = \frac{\sigma_j}{\sigma_{j+1}}\left(\zeta\varphi'_j(\zeta) - \frac{1}{r_j}\Phi_j\left(\frac{\zeta}{r_j^2}\right) - \frac{\zeta}{r_j^3}\Phi'_{j-1}\left(\frac{\zeta}{r_j^2}\right)\right),$$

then the equations (19) and (20) read:

$$\begin{cases} \varphi_{j+1}(\zeta) + \dfrac{1}{r_j}\Phi_{j+1}\left(\dfrac{\zeta}{r_j^2}\right) = f_j(\zeta), \\ \zeta\varphi'_{j+1} - \dfrac{1}{r_j}\Phi_{j+1}\left(\dfrac{\zeta}{r_j^2}\right) - \dfrac{\zeta}{r_j^3}\Phi'_{j+1}\left(\dfrac{\zeta}{r_j^2}\right) = g_j(\zeta). \end{cases} \tag{21}$$

By elimination of φ_{j+1} in (21), we obtain an ordinary differential equation (ODE) for Φ_{j+1}:

$$\frac{2\zeta}{r_j^3}\Phi'_{j+1}\left(\frac{\zeta}{r_j^2}\right) + \frac{1}{r_j}\Phi_{j+1}\left(\frac{\zeta}{r_j^2}\right) = -g_j(\zeta) + \zeta f'_j(\zeta).$$

Once the above ODE is solved, and thus Φ_{j+1} is known, we can find φ_{j+1} by solving the first equation of (21) for φ_{j+1}:

$$\varphi_{j+1} = f_j(\zeta) - \frac{1}{r_j}\Phi_{j+1}\left(\frac{\zeta}{r_j^2}\right),$$

which concludes this proof. □

So, if we choose φ_1 and Φ_1, we can construct $\psi\big|_{\partial\Omega}$ by (repeated) propagation of φ_j and Φ_j through the boundaries $\partial\Omega_j$ until we reach the outer boundary. Note that the ODE that defines Φ_{j+1} can be integrated exactly.

The ODE that defines Φ_{j+1} can be integrated exactly when we propagate the logarithmic function (8) from the deepest ring, $\Omega_1 = \{\mathbf{x} \in \mathbb{R}^3, \text{ s.t. } \|\mathbf{x}\| \leq r_1\}$ which contains the origin $(0,0,0)$. However, this expression is quite complicated and not very informative. A better alternative is to work directly with the power series expansion of Φ_j and φ_j.

Proposition 2. *Assume that, in the ring Ω_j, the functions φ_j and Φ_j can be expressed using the following power series expansion*

$$\varphi_j(\zeta) = \sum_{k\geq 0} c_{j,k}\zeta^k$$
$$\Phi_j(\zeta) = \sum_{k\geq 0} d_{j,k}\zeta^k$$

Then, the coefficients $c_{j,k}, d_{j,k}$ satisfy a linear induction over the index j

$$\begin{pmatrix} c_{j+1,k} \\ \\ d_{j+1,k} \end{pmatrix} = \begin{pmatrix} 1-u_{j,k} & v_{j,k}r_j^{-2k-1} \\ \\ u_{j,k}r_j^{2k+1} & 1-v_{j,k} \end{pmatrix} \begin{pmatrix} c_{j,k} \\ \\ d_{j,k} \end{pmatrix} \tag{22}$$

where

$$u_{j,k} = \frac{k}{2k+1}\Big(1 - \frac{\sigma_j}{\sigma_{j+1}}\Big) \quad \textit{and} \quad v_{j,k} = \frac{k+1}{2k+1}\Big(1 - \frac{\sigma_j}{\sigma_{j+1}}\Big).$$

If the function $\psi(\zeta)$ is equal to $\log(1-\zeta/a_n)$ in Ω_1, we can initialize this induction formula with

$$c_{1,k} = \begin{cases} -\frac{1}{ka_n^k} & \textit{for } k \geq 1 \\ 0 & \textit{otherwise} \end{cases} \qquad \textit{and } d_{1,k} = 0,\ \forall k \geq 0$$

Proof. Across $\partial\Omega_j$, the function $\psi(\zeta) = \varphi_j(\zeta) + \frac{1}{r}\Phi_j\left(\frac{\zeta}{r^2}\right)$ is continuous as well as $\sigma\nabla\psi \cdot \mathbf{e}_{\partial\Omega_j}$. Using the power series expression of $\psi(\zeta)$, we thus have

$$\begin{aligned}
\sum_{k\geq 0} c_{j,k}\zeta^k + \sum_{k\geq 0} \frac{d_{j,k}}{r_j^{2k+1}}\zeta^k &= \sum_{k\geq 0} c_{j+1,k}\zeta^k + \sum_{k\geq 0} \frac{d_{j+1,k}}{r_j^{2k+1}}\zeta^k \\
\sigma_j \sum_{k\geq 0} k c_{j,k}\zeta^k - \sigma_j \sum_{k\geq 0} (k+1)\frac{d_{j,k}}{r_j^{2k+1}}\zeta^k &= \sigma_{j+1} \sum_{k\geq 0} k c_{j+1,k}\zeta^k - \sigma_{j+1} \sum_{k\geq 0} (k+1)\frac{d_{j+1,k}}{r_j^{2k+1}}\zeta^k
\end{aligned}$$

After identifying left and right coefficients of ζ^k we obtain two equations for each k, which can be put under matrix form

$$\begin{pmatrix} 1 & \frac{1}{r_j^{2k+1}} \\ k\sigma_j & -\frac{(k+1)\sigma_j}{r_j^{2k+1}} \end{pmatrix} \begin{pmatrix} c_{j,k} \\ d_{j,k} \end{pmatrix} = \begin{pmatrix} 1 & \frac{1}{r_j^{2k+1}} \\ k\sigma_{j+1} & -\frac{(k+1)\sigma_{j+1}}{r_j^{2k+1}} \end{pmatrix} \begin{pmatrix} c_{j+1,k} \\ d_{j+1,k} \end{pmatrix}$$

After a few simple algebraic manipulations this is equivalent to (22). The appendices show the construction of ψ_3 and ϕ_3, explicitly, using proposition 1. This may considerably help the implementation.

□

4. **A note on non-spherical mediums.** In the case of a non-homogeneous medium, we only need to assume that σ is constant within the potential support, Ω_0, of ρ. In EEG, for example, the generating sources lie in the grey matter for which the conductivity does not vary. In that case, we may still choose the test functions to be of the form $\log(1-(x+iy)/a)$ in Ω_0. Then the test functions can be propagated to the boundary of the volume model in such a way as to satisfy $\mathrm{div}(\sigma\nabla\psi) = 0$ using numerical techniques such as finite element methods [22] or boundary element methods (for domains with piecewise constant σ) [23]. The propagation of the test functions up to the volume conductor's boundary implicitly encodes the information of the forward model in more complex configurations. Consequently, the generalized samples also take into account the presence of the non-spherical medium. The localization method, presented briefly in section 2.3, remains identical.

5. **A simulation study.**

5.1. **Spherical head model with multiple layers.** A common head model in EEG applications is the 3-sphere conductivity model [4, 34, 38] depicted in Fig. 1. Each compartment Ω_1, Ω_2 and Ω_3, with their respective conductivities σ_1, σ_2 and σ_3, represents a specific tissue class. In the case of the 3-sphere model the compartments represent the brain tissue, skull and scalp, respectively. It is generally accepted that the brain and scalp tissue have a comparable conductivity ($\sigma_1 = \sigma_3$), whereas the skull has a much lower conductivity (e.g., $\frac{\sigma_1}{\sigma_2} = 80$). Such a compartment with low conductivity attenuates and smooths the generated boundary potential $V\big|_{\partial\Omega}$. Figure 2 demonstrates this attenuation and blurring due to the layer Ω_2 with low conductivity. For the remaining of this paper, we use the 3-sphere conductivity model with $r_1 = 0.86, r_2 = 0.92, r_3 = 1$ and $\sigma_1 = 1, \sigma_2 = 0.0125, \sigma_3 = 1$ as in the commonly used SMAC head model [34].

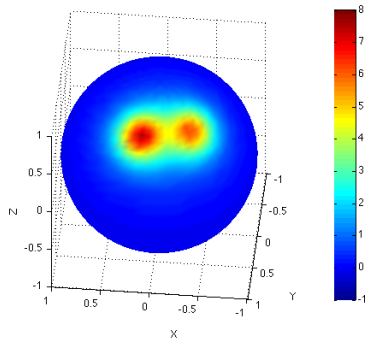

(a)

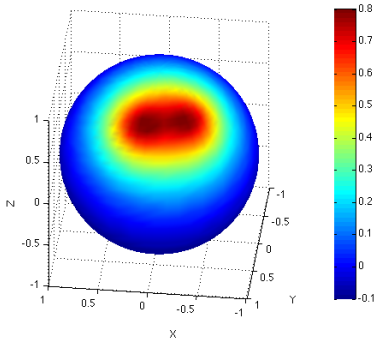

(b)

FIGURE 2. (a) $V\big|_{\partial\Omega}$ generated by a source distribution ρ in a homogeneous ($\sigma = 1$) sphere. (b) $V\big|_{\partial\Omega_3}$ generated by the same source distribution in a 3-sphere conductivity model. The different compartments represent the brain tissue (radius $r_1 = 0.86$ and conductivity $\sigma_1 = 1$), the skull ($r_2 = 0.92$ and $\sigma_2 = 0.0125$), and the scalp ($r_3 = 1$ and $\sigma_3 = 1$). The source distribution contains two dipoles with positions $\mathbf{x}_1 = [0.1\ 0.5\ 0.6]^{\mathrm{T}}$, $\mathbf{x}_2 = [-0.3\ 0.4\ 0.6]^{\mathrm{T}}$, and moments $\mathbf{p_1} = \frac{\mathbf{x}_1}{||\mathbf{x}_1||}$ and $\mathbf{p_2} = \frac{\mathbf{x}_2}{||\mathbf{x}_2||}$.

5.2. **Propagation of analytic sensors.** We propagate the analytic sensor ψ_{a_n} in Ω_1 through the boundaries $\partial\Omega_1$ and $\partial\Omega_2$ of the compartments Ω_1 and Ω_2, respectively, taking into account the conductivity profile. Appendices A and B include the detailed derivation and lead to the closed-form expression of ψ at the outer boundary that can then be used to compute the generalized measures. In Fig. 3, we show a vector-field representation of the analytic sensor for the homogeneous and the multi-layer spherical model. On this example, we observe that the essential effect of the conductivity change is to increase the contrast between homogenous regions, but not to modify significantly the localization pattern in the neighborhood of the sensor location.

5.3. **Localization performance.** Finally, we demonstrate the importance of the analytic sensors that take into account the conductivity profile of the conductivity

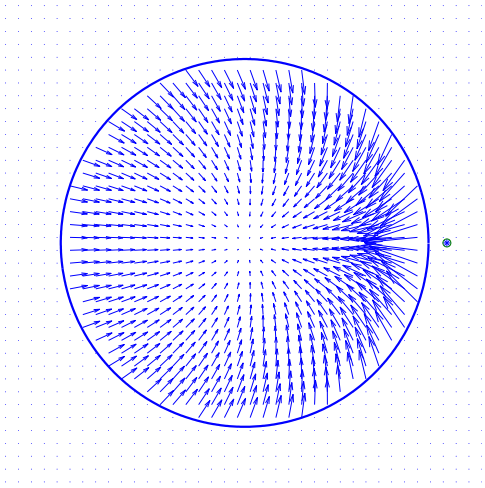

(a)

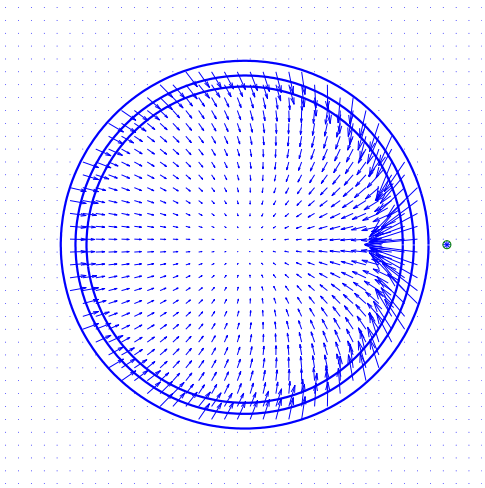

(b)

FIGURE 3. (a) Vector-field representation in the (x, y)-plane of the analytic sensor function $\log(1-(x+iy)/1.1)$ for the homogeneous conductivity model. (b) Vector-field representation of the same analytic sensor, but that propagates through three layers with different conductivities as described in Sect. 5.1. The phase and the amplitude of the complex-valued analytic sensor determines the orientation and the length of the vector, respectively.

model. To that aim, we compute the potential generated by a unit dipole that is oriented outwards and perpendicular to the spherical surface (i.e., $\mathbf{p_1} = \frac{\mathbf{x}_1}{||\mathbf{x}_1||}$), at randomly chosen locations $\mathbf{x}_1$. The measurements are taken at 204 electrodes of a high-density EEG cap mapped on the 3-sphere conductivity model, as illustrated in Fig. 5.3. We used 32 analytic sensors $\{\psi_{a_n}\}_{n=0\cdots31}$ with singularities $a_n =$

$1.1\exp(i\frac{2\pi}{32}n)$. The analytic sensors use the exact radii ($r_1 = 0.86, r_2 = 0.92$) and conductivities ($\sigma_1 = 1$ and $\sigma_3 = 1$) of the inner layer boundaries. We varied the conductivity σ_2 taken into account by the analytic sensors. For each variation of σ_2 we computed $\langle \psi_{a_n}, \rho \rangle$ and performed a localization using the annihilating-filter approach [21]. We repeated the experiment 100 times to obtain a standard deviation of the localization error. Note that, in order to compute the generalized measures, we need to represent the boundary potential in a continuous way. For this, we used a thin-plate spline interpolation [15]. Then, Matlab's dblquad, which uses a recursive adaptive Simpson quadrature, was used to compute the generalized measures (4).

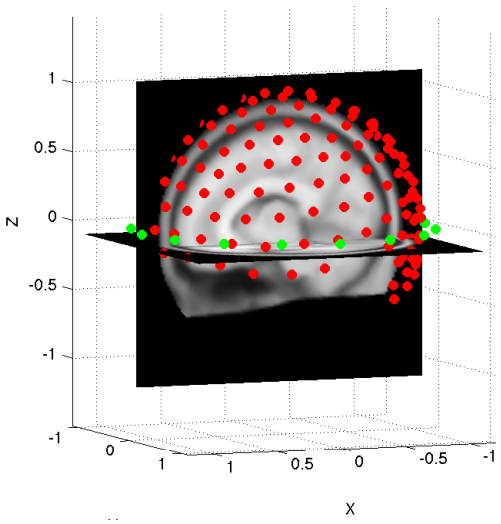

FIGURE 4. Illustration of the setup that was used to perform the simulations. The conductivity model is a 3-layer spherical model. The red dots indicate the electrodes at the outer boundary and the green dots the singularities a_n of the analytic sensors ψ_{a_n}.

Varying σ_2 in the analytic sensors introduces a model mismatch between the conductivity profile used to generate the boundary potential and the conductivity profile taken into account by the analytic sensors which in turn influences the localization error. Figures 5(a) and 5(b) depict the effect of a varying σ_2, taken into account by the analytic sensors, on the localization error. We see that the localization error ($||\mathbf{x}_{estim} - \mathbf{x}_1||$) is minimal if there is no model mismatch between the conductivity profile used to generate the boundary potential and the conductivity profile taken into account by the analytic sensors. Hence, in our case, the localization error is minimal if we construct ψ_{a_n} such that it accounts for $\sigma_1 = 1, \sigma_2 = 0.0125$ and $\sigma_3 = 1$.

As a side note, we would like to emphasize that the number of electrodes, N, plays some role in the resulting localization error [27]. More specifically, it is possible to compute theoretical lower bounds for the variance of the error on the (x, y, z) localization of the dipoles—Cramér-Rao bounds. We have experimentally observed that our algorithm reaches these bounds (see [20, Chapter 7.3]). Figures 6(a) and 6(b)

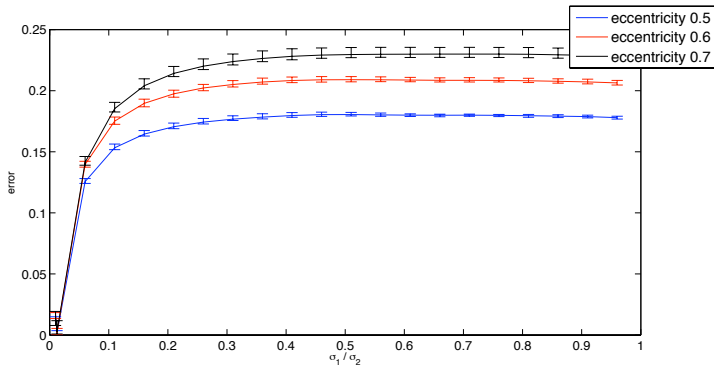

(a)

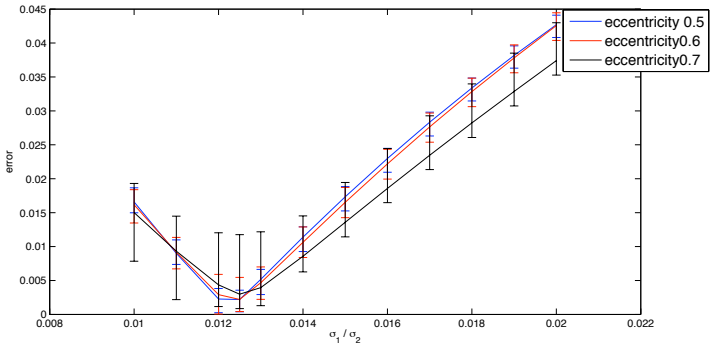

(b)

FIGURE 5. Mean localization error ($||\mathbf{x_{estimate}} - \mathbf{x_1}||$) as a function of the inexact conductivity profile σ_2/σ_1 taken into account by the analytic sensors and the actual conductivity profile ($= 0.0125$) used to generate the boundary potential. Furthermore, the maximum and minimum localization error is depicted by means of error bars. The boundary potential is generated by unit dipoles at different distances from the center (eccentricity), $||\mathbf{x_1}||$, and measured at 204 electrodes on $\partial\Omega_3$. Figure 5(b) is the enlargement of figure 5(a) for $0.008 < \frac{\sigma_2}{\sigma_1} < 0.022$.

depict these minimal errors in function of the noise level (assuming additive Gaussian noise), for a 64 and a 204 electrode setup. As could be expected increasing the number of electric potential measurements makes the localization more accurate. Here we added noise to the generalized measures, but we observed similar behavior when degrading the boundary measurements directly.

In some cases such a parameterization reflects the true underlying source distribution accurately, e.g., in some cases of partial epilepsy. However, often the activations are in fact small patches of many dipoles. In such cases the proposed model is a good approximation of the true source distribution.

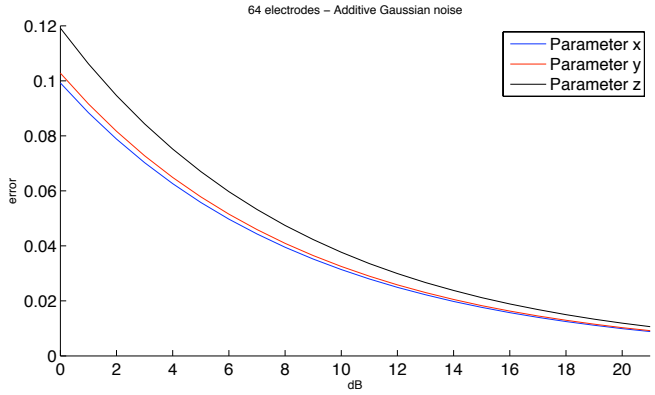

(a)

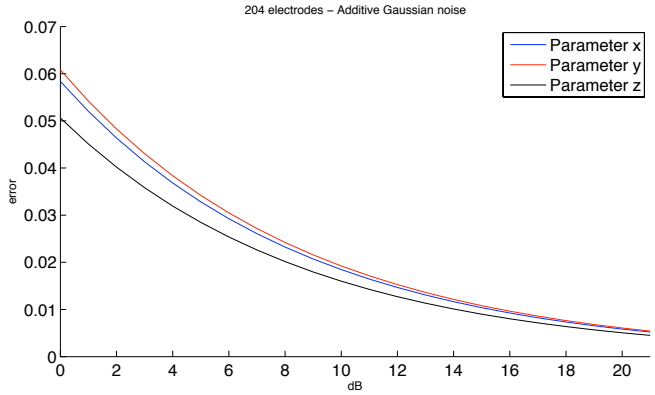

(b)

FIGURE 6. Lower bound on the localization error in function of the noise level (assuming additive Gaussian noise) for $N = 64$ (a) and $N = 204$ (b) electrodes. The noise level is measured as signal-to-noise ratio in dB.

6. **Conclusion.** We proposed an extension of the sensing principle to account for a multi-layer spherical conductivity model. In order to construct the desired analytic sensors, we solved Poisson's equation, $\operatorname{div}(\sigma\nabla\psi) = 0$, with σ radially piecewise constant. We have shown that, in the case of a N-sphere conductivity model, we can propagate ψ analytically.

We should mention that the proposed method does not provide the final solution to EEG/MEG source localization. Indeed, our hypotheses (piecewise constant spherical conductivity, point-source model) are grossly violated in any practical setting. Yet, we expect our approach to be a reasonably acceptable, and hopefully useful, low-dimensional approximation (i.e., for few significant dipoles) of the more complex physiological situation, in particular when the activation loci are clustered.

Acknowledgements. This work was supported in part by the Swiss National Science Foundation grants 200020-109415, 205320-132808, and PP00P2-123438, in part

by the Sino-Swiss Science and Technology Cooperation Program (EG03-092008), in part by the Microsoft-Chinese University of Hong Kong (CUHK) Joint Laboratory Research Student Grant, and in part by an RGC grant #CUHK410110 of the Hong Kong University Grant Council.

Finally, we like to acknowledge the Center for Biomedical Imaging (CIBM) of the Geneva-Lausanne Universities and the EPFL as well as the foundations Leenaards and Louis-Jeantet.

Appendix A. **Propagation through $\partial\Omega_1$.** Consider the functions φ_1 and Φ_1 which are defined from the center up to the boundary $\partial\Omega_1$ of the 3-sphere conductivity model $\mathcal{S}$ (depicted in Fig. 1):

$$\begin{aligned} \varphi_1(\zeta) &= \log(1-\zeta/a), \\ \Phi_1(\frac{\zeta}{r^2}) &= 0, \end{aligned}$$

with $a \notin \mathcal{S}$. Next, we define the functions f_1 and g_1 as stated in equations (17) and (18):

$$\begin{aligned} f_1(\zeta) &= \log(1-\zeta/a), \\ g_1(\zeta) &= \frac{\sigma_1}{\sigma_2}\frac{\zeta}{\zeta-a}. \end{aligned}$$

In order to propagate Φ_1 trough the boundary Ω_1, which yield Φ_2, we need to solve the ODE (15) for $j=1$:

$$\frac{2\zeta}{r_1^3}\Phi_2'\left(\frac{\zeta}{r_1^2}\right) + \frac{1}{r_1}\Phi_2\left(\frac{\zeta}{r_1^2}\right) = -g_1(\zeta) + \zeta f_1'(\zeta). \tag{23}$$

Since Φ_2 is analytic, we can write:

$$\Phi_2\left(\frac{\zeta}{r_1^2}\right) = \sum_{k\geq 0} c_k \left(\frac{\zeta}{r_1^2}\right)^k. \tag{24}$$

For the rhs of the ODE (23), we have:

$$\begin{aligned} -g_1(\zeta) + \zeta f_1'(\zeta) &= \left(1-\frac{\sigma_1}{\sigma_2}\right)\frac{\zeta}{\zeta-a}, \\ &= \left(\frac{\sigma_1}{\sigma_2}-1\right)\sum_{k\geq 0}\left(\frac{\zeta}{a}\right)^{k+1}. \end{aligned} \tag{25}$$

If we substitute the expressions (24) and (25) in the ODE (23), then we obtain:

$$\sum_{k\geq 0} c_k \frac{2k+1}{r_1^{2k+1}}\zeta^k = \left(\frac{\sigma_1}{\sigma_2}-1\right)\sum_{k\geq 0}\left(\frac{\zeta}{a}\right)^{k+1},$$

from which we infer the coefficients c_k:

$$\begin{aligned} c_0 &= 0, \\ c_k &= \left(\frac{\sigma_1}{\sigma_2}-1\right)\frac{r_1^{2k+1}}{(2k+1)a^k}, \quad \text{for } k \geq 1. \end{aligned}$$

This yields the following expression for Φ_2:

$$\Phi_2\left(\frac{\zeta}{r^2}\right) = \left(\frac{\sigma_1}{\sigma 2}-1\right)\sum_{k\geq 1}\frac{r_1^{2k+1}}{(2k+1)a^k}\left(\frac{\zeta}{r^2}\right)^k.$$

If we set $j = 1$ in equation (16), then we obtain an expression for φ_2:

$$\begin{aligned}\varphi_2(\zeta) &= f_1(\zeta) - \frac{1}{r_1}\Phi_2\left(\frac{\zeta}{r_1^2}\right), \\ &= \log(1-\zeta/a) - \left(\tfrac{\sigma_1}{\sigma 2} - 1\right)\sum_{k\geq 1}\frac{\zeta^k}{(2k+1)a^k}.\end{aligned}$$

Appendix B. **Propagation through $\partial\Omega_2$.** Consider the functions φ_2 and Φ_2 (as constructed in the previous appendix) which are defined from the center up to the boundary $\partial\Omega_2$ of the 3-sphere conductivity model $\mathcal{S}$ (depicted in Fig. 1):

$$\begin{aligned}\varphi_2(\zeta) &= \log(1-\zeta/a) - \left(\tfrac{\sigma_1}{\sigma 2} - 1\right)\sum_{k\geq 1}\frac{\zeta^k}{(2k+1)a^k} \\ \Phi_2\left(\tfrac{\zeta}{r^2}\right) &= \left(\tfrac{\sigma_1}{\sigma 2} - 1\right)\sum_{k\geq 1}\frac{r_1^{2k+1}}{(2k+1)a^k}\left(\frac{\zeta}{r^2}\right)^k,\end{aligned}$$

with $a \notin \mathcal{S}$. Next, we define the functions f_2 and g_2 as stated in equations (17) and (18):

$$\begin{aligned}f_2(\zeta) &= \log(1-\zeta/a) - \left(\frac{\sigma_0}{\sigma_1} - 1\right)\sum_{k\geq 1}\left(1 - \frac{r_1^{2k+1}}{r_2^{2k+1}}\right)\frac{1}{(2k+1)a^k}\zeta^k \\ g_2(\zeta) &= -\frac{\sigma_2}{\sigma_3}\sum_{k\geq 1}\left(\frac{1}{a^k} + \left(\frac{\sigma_1}{\sigma_2} - 1\right)\frac{k}{(2k+1)a^k} + \left(\frac{\sigma_1}{\sigma_2} - 1\right)\frac{(k+1)r_1^{2k+1}}{(2k+1)a^k r_2^{2k+1}}\right)\zeta^k\end{aligned}$$

In order to propagate Φ_2 trough the boundary Ω_2, which yield Φ_3, we need to solve the ODE (15) for $j = 2$:

$$\frac{2\zeta}{r_2^3}\Phi_3'\left(\frac{\zeta}{r_2^2}\right) + \frac{1}{r_2}\Phi_3\left(\frac{\zeta}{r_2^2}\right) = -g_2(\zeta) + \zeta f_2'(\zeta). \tag{26}$$

Since Φ_3 is analytic, we can write:

$$\Phi_3\left(\frac{\zeta}{r_2^2}\right) = \sum_{k\geq 0} c_k\left(\frac{\zeta}{r_2^2}\right)^k. \tag{27}$$

For the rhs of the ODE (26), we have:

$$\begin{aligned}-g_2(\zeta) + \zeta f_2'(\zeta) &= \left(\tfrac{\sigma_2}{\sigma_3} - 1\right)\sum_{k\geq 1}\frac{\zeta^k}{a^k} + \\ &\quad \left(\tfrac{\sigma_1}{\sigma_2} - 1\right)\left(\tfrac{\sigma_2}{\sigma_3} - 1\right)\sum_{k\geq 1}\frac{k}{2k+1}\left(\frac{\zeta}{a}\right)^k + \\ &\quad \left(\tfrac{\sigma_1}{\sigma_2} - 1\right)\sum_{k\geq 1}\frac{\left(\tfrac{\sigma_2}{\sigma_3}(k+1) + k\right)r_1^{2k+1}}{(2k+1)r_2^{2k+1}}\left(\frac{\zeta}{a}\right)^k.\end{aligned} \tag{28}$$

If we substitute the expressions (27) and (28) in the ODE (26), then we obtain:

$$\begin{aligned}\textstyle\sum_{k\geq 0} c_k\frac{2k+1}{r_2^{2k+1}}\zeta^k &= \left(\tfrac{\sigma_2}{\sigma_3} - 1\right)\textstyle\sum_{k\geq 1}\frac{\zeta^k}{a^k} + \\ &\quad \left(\tfrac{\sigma_1}{\sigma_2} - 1\right)\left(\tfrac{\sigma_2}{\sigma_3} - 1\right)\textstyle\sum_{k\geq 1}\frac{k}{2k+1}\left(\frac{\zeta}{a}\right)^k + \\ &\quad \left(\tfrac{\sigma_1}{\sigma_2} - 1\right)\textstyle\sum_{k\geq 1}\frac{\left(\tfrac{\sigma_2}{\sigma_3}(k+1) + k\right)r_1^{2k+1}}{(2k+1)r_2^{2k+1}}\left(\frac{\zeta}{a}\right)^k,\end{aligned}$$

from which we infer the coefficients c_k:

$$\begin{aligned} c_0 &= 0, \\ c_k &= \left(\frac{\sigma_2}{\sigma_3}-1\right)\frac{r_2^{2k+1}}{(2k+1)a^k} + \left(\frac{\sigma_1}{\sigma_2}-1\right)\left(\frac{\sigma_2}{\sigma_3}-1\right)\frac{kr_2^{2k+1}}{(2k+1)^2a^k} + \\ &\quad \left(\frac{\sigma_1}{\sigma_2}-1\right)\frac{\left(\frac{\sigma_2}{\sigma_3}(k+1)+k\right)r_1^{2k+1}}{(2k+1)^2a^k}, \quad \text{for } k \geq 1. \end{aligned}$$

This yields the following expression for Φ_3:

$$\begin{aligned} \Phi_3\left(\tfrac{\zeta}{r^2}\right) &= \left(\tfrac{\sigma_2}{\sigma_3}-1\right)\sum_{k\geq 1}\frac{r_2^{2k+1}}{(2k+1)a^k}\left(\frac{\zeta}{r^2}\right)^k + \\ &\quad \left(\tfrac{\sigma_1}{\sigma_2}-1\right)\left(\tfrac{\sigma_2}{\sigma_3}-1\right)\sum_{k\geq 1}\frac{kr_2^{2k+1}}{(2k+1)^2a^k}\left(\frac{\zeta}{r^2}\right)^k + \\ &\quad \left(\tfrac{\sigma_1}{\sigma_2}-1\right)\sum_{k\geq 1}\frac{\left(\frac{\sigma_2}{\sigma_3}(k+1)+k\right)r_1^{2k+1}}{(2k+1)^2a^k}\left(\frac{\zeta}{r^2}\right)^k \end{aligned}$$

If we set $j = 2$ in equation (16), then we obtain an expression for φ_3:

$$\begin{aligned} \varphi_3(\zeta) &= f_2(\zeta) - \frac{1}{r_2}\Phi_3\left(\frac{\zeta}{r_2^2}\right), \\ &= \log(1-\zeta/a) - \left(\tfrac{\sigma_1}{\sigma_2}-1\right)\sum_{k\geq 1}\left(1-\left(\frac{r_1}{r_2}\right)^{2k+1}\right)\frac{\zeta^k}{(2k+1)a^k} - \\ &\quad \left(\tfrac{\sigma_2}{\sigma_3}-1\right)\sum_{k\geq 1}\frac{\zeta^k}{(2k+1)a^k} - \left(\frac{\sigma_1}{\sigma_2}-1\right)\left(\frac{\sigma_2}{\sigma_3}-1\right)\sum_{k\geq 1}\frac{k\zeta^k}{(2k+1)^2a^k} - \\ &\quad \left(\tfrac{\sigma_1}{\sigma_2}-1\right)\sum_{k\geq 1}\frac{\left(\frac{\sigma_2}{\sigma_3}(k+1)+k\right)r_1^{2k+1}}{(2k+1)^2a^kr_2^{2k+1}}\zeta^k, \end{aligned}$$

which yields an expression for $\psi_a(\zeta, r) = \varphi_3(\zeta) + \frac{1}{r}\Phi_3\left(\frac{\zeta}{r^2}\right)$.

REFERENCES

[1] S. Andrieux, T. N. Baranger, and A. Ben Abda. Solving Cauchy problems by minimizing an energy-like functional. *Inverse Problems*, 22(1):115–133, 2006.

[2] S. Andrieux and A. Ben Abda. The reciprocity gap: A general concept for flaws identification problems. *Mechanical Research Communications*, 20(5):415–420, 1993.

[3] S. Andrieux, A. Ben Abda, and J. Mohamed. On the inverse emergent plane crack problem. *Mathematical Methods in the Applied Sciences*, 21(10):895–906, 1998.

[4] J. P. Ary, S. A. Klein, and D. H. Fender. Location of sources of evoked scalp potentials: Corrections for skull and scalp thicknesses. *IEEE Transactions on Biomedical Engineering*, BME-28(6):447–452, 1981.

[5] K. A. Awada, D. R. Jackson, S. B. Baumann, B. Stephen, J. T. Williams, D. R. Wilton, P. Fink, and B. Prasky. Effect of conductivity uncertainties and modeling errors on EEG source localization using a 2-D model. *IEEE Transactions on Biomedical Engineering*, 45(9):1135–1145, 1998.

[6] S. Baillet, J. C. Mosher, and R. M. Leahy. Electromagnetic brain mapping. *IEEE Signal Processing Magazine*, 18(6):14–30, 2001.

[7] L. Baratchart, A. Ben Abda, F. Ben Hassen, and J. Leblond. Recovery of pointwise sources or small inclusions in 2D domains and rational approximation. *Inverse problems*, 21:51–74, 2005.

[8] L. Baratchart, J. Leblond, and J. P. Marmorat. Inverse sources problem in a 3D ball from best meromorphic approximation on 2D slices. *Electronic Transactions on Numerical Analysis*, 25:41–53, 2006.

[9] G. R. Barnes and A. Hillebrand. Statistical flattening of MEG beamformer images. *Human Brain Mapping*, 18:1–12, 2003.

[10] G. Birot, L. Albera, F. Wendling, and I. Merlet. Localisation of extended brain sources from EEG/MEG: the ExSo-MUSIC approach. *NeuroImage*, 2011.

[11] T. Blu, P.-L. Dragotti, M. Vetterli, P. Marziliano, and L. Coulot. Sparse sampling of signal innovations. *IEEE Signal Processing Magazine*, 25(2):31–40, 2008.

[12] M. Clerc and J. Kybic. Cortical mapping by Laplace-Cauchy transmission using a boundary element method. *Inverse Problems*, 23(6):2589–2601, 2007.

[13] B. N. Cuffin. Effects of head shape on EEG's and MEG's. *IEEE Transactions On Biomedical Engineering*, 37(1):44–52, 1990.

[14] A. El Badia and T. Ha-Duong. An inverse source problem in potential analysis. *Inverse Problems*, 16(3):651–663, 2000.

[15] G. E. Fasshauerand. *Mathematical Methods For Curves And Surfaces II*. Vanderbilt University Press, 1998.

[16] D. B. Geselowitz. On bioelectric potentials in an inhomogeneous volume conductor. *Biophysical Journal*, 7(1):1–11, 1967.

[17] D. Gutirrez and A. Nehorai. Estimating brain conductivities and dipole source signals with EEG arrays. *IEEE Transactions On Biomedical Engineering*, 51(12):2113–2122, 2004.

[18] H. L. F. Helmholtz. Über Einige Gesetze der Vertheilung Elektrischer Ströme in Köperlichen Leitern mit Anwendung auf die Thierisch-Elektrischen Versuche. *Annalen der Physik*, 9:211–233, 1853.

[19] V. Isakov. *Inverse Source Problems*, volume 34 of *Mathematical Surveys and Monographs Series*. AMS, Providence, RI, 1990.

[20] D. Kandaswamy. *Analytic Sensing: Sparse Source Recovery From Boundary Measurements Using An Extension Of Prony's Method For The Poisson Equation*. PhD thesis, École Polytechnique Fédérale de Lausanne, 2011.

[21] D. Kandaswamy, T. Blu, and D. Van De Ville. Analytic sensing: Noniterative retrieval of point sources from boundary measurements. *SIAM Journal on Scientific Computing*, 31(4):3179–3194, 2009.

[22] V. A. Kozlov, V. G. Maz'ya, and A. V. Fomin. An iterative method for solving the Cauchy problem for elliptic equations. *Comput. Math. Phys.*, 31:45–52, 1991.

[23] J. Kybic, M. Clerc, T. Abboud, O. Faugeras, R. Keriven, and T. Papadopoulo. A common formalism for the integral formulations of the forward EEG problem. *IEEE Transactions on Medical Imaging*, 24:12–28, 2005.

[24] J. Kybic, M. Clerc, O. Faugeras, R. Keriven, and T. Papadopoulo. Fast multipole acceleration of the MEG/EEG boundary element method. *Physics in Medicine and Biology*, 50(19):4695–4710, 2005.

[25] J. Kybic, M. Clerc, O. Faugeras, R. Keriven, and T. Papadopoulo. Generalized head models for MEG/EEG: Boundary element method beyond nested volumes. *Physics in Medicine and Biology*, 51(5):13333–1346, 2006.

[26] C. M. Michel, G. Lantz, L. Spinelli, R. Grave de Peralta, T. Landis, and M. Seeck. 128-channel EEG source imaging in epilepsy: Clinical yield and localization precision. *J Clin Neurosphysiol*, 21:71–83, 2004.

[27] C. M. Michel, M. M. Murray, G. Lantz, S. Gonzalez, L. Spinelli, and R. Grave de Peralta. EEG source imaging. *Clin Neurophysiol*, 115(10):2195–2222, 2004.

[28] K. Miller. Stabilized numerical prolongation with poles. *SIAM J. Appl. Math.*, 18(2):346–363, 1970.

[29] S. Mingui. An efficient algorithm for computing multishell spherical volume conductor models in EEG dipole source localization. *IEEE Transactions On Biomedical Engineering*, 44(12):1243–1252, 1997.

[30] J. C. Mosher, P. S. Lewis, and R. M. Leahy. Multiple dipole modeling and localization from spatio-temporal MEG data. *IEEE Transactions on Biomedical Engineering*, 39:541–557, 1992.

[31] T. Nara and S. Ando. A projective method for an inverse source problem of the Poisson equation. *Inverse Problems*, 19(2):355–369, 2003.

[32] M. Scherg and D. von Cramon. Two bilateral sources of the late AEP as identied by a spatio-temporal dipole model. *Electroenceph Clinic Neurophysiol*, 62:290–299, 1985.
[33] D. M. Schmidt, J. S. George, and C. C. Wood. Bayesian inference applied to the electromagnetic inverse problem. *Human Brain Mapping*, 7:195–212, 1999.
[34] L. Spinelli, S. G. Andino, G. Lantz, M. Seeck, and C. M. Michel. Electromagnetic inverse solutions in anatomically constrained spherical head models. *Brain Topography*, 13(2), 2000.
[35] V. Srinivasan, C. Eswaran, and N. Sriraam. Approximate entropy-based epileptic EEG detection using artificial neural networks. *IEEE Transactions On Information Technology In Biomedicine*, 11(3):288–295, 2007.
[36] O. Steinstrter, S. Sillekens, M. Junghoefer, M. Burger, and C.H. Wolters. Sensitivity of beamformer source analysis to deficiencies in forward modeling. *Human Brain Mapping*, 31(12):1907–1927, 2010.
[37] A. N. Tikhonov. On the stability of inverse problems. *Dokl. Akad. Nauk SSSR*, 39(5):195–198, 1943.
[38] S. Vallaghe and M. Clerc. A global sensitivity analysis of three- and four-layer EEG conductivity models. *IEEE Transactions on Biomedical Engineering*, 56(4):998–995, 2009.
[39] B. Vanrumste, G. Van Hoey, R. Van de Walle, M. D'Have, I. Limahieu, and P. Boon. Dipole location errors in electroencephalogram source analysis due to volume conductor model errors. *Medical & Biological Engineering & Computing*, 38(5):528–534, 2000.
[40] M. Vetterli, P. Marzilliano, and T. Blu. Sampling signals with finite rate of innovation. *IEEE Transactions on Signal Processing*, 50(6):1417–1428, 2002.
[41] D. P. Wipf, J. P. Owena, H. T. Attiasb, K. Sekiharac, and S. S. Nagarajana. Robust Bayesian estimation of the location, orientation, and time course of multiple correlated neural sources using MEG. *NeuroImage*, 49(1):641–655, 2010.

Received xxxx 20xx; revised xxxx 20xx.

E-mail address: Django.Kandaswamy@gmail.com
E-mail address: Thierry.Blu@m4x.org
E-mail address: Dimitri.VanDeVille@epfl.ch